JCI insight

Molecular and cellular context influences *SCN8A* variant function

Carlos G. Vanoye, … , Christopher H. Thompson, Alfred L. George Jr.

JCI Insight. 2024;9(12):e177530. https://doi.org/10.1172/jci.insight.177530.

Research Article Genetics Neuroscience

Graphical abstract

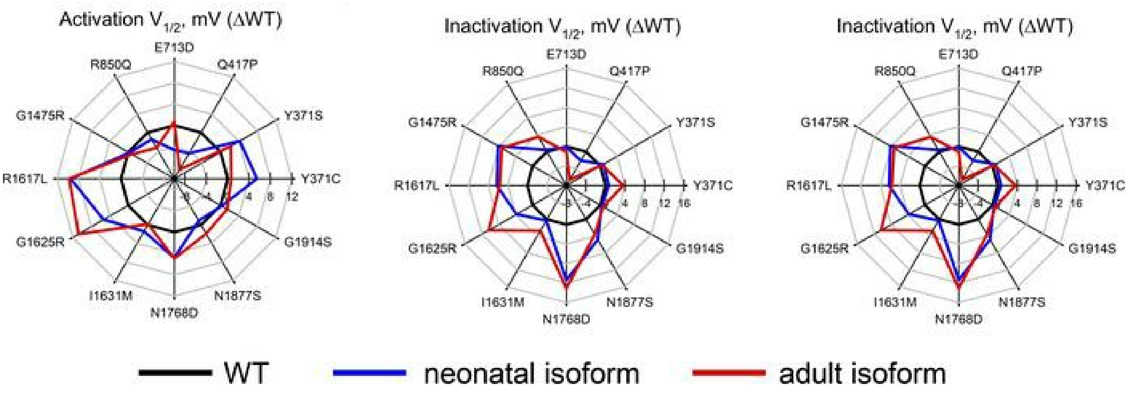

JCI insight

Molecular and cellular context influences *SCN8A* variant function

Carlos G. Vanoye,[1] Tatiana V. Abramova,[1] Jean-Marc DeKeyser,[1] Nora F. Ghabra,[1] Madeleine J. Oudin,[2] Christopher B. Burge,[3] Ingo Helbig,[4,5] Christopher H. Thompson,[1] and Alfred L. George Jr.[1]

[1]Department of Pharmacology, Northwestern University Feinberg School of Medicine, Chicago, Illinois, USA. [2]Department of Biomedical Engineering, Tufts University, Medford, Massachusetts, USA. [3]Department of Biology, Massachusetts Institute of Technology, Cambridge, Massachusetts, USA. [4]Division of Neurology, Children's Hospital of Philadelphia, Philadelphia, Pennsylvania, USA. [5]Department of Neurology, Perelman School of Medicine, University of Pennsylvania, Philadelphia, Pennsylvania, USA.

Pathogenic variants in *SCN8A*, which encodes the voltage-gated sodium (Na_V) channel Na_V1.6, associate with neurodevelopmental disorders, including developmental and epileptic encephalopathy. Previous approaches to determine *SCN8A* variant function may be confounded by use of a neonatally expressed, alternatively spliced isoform of Na_V1.6 (Na_V1.6N) and engineered mutations rendering the channel tetrodotoxin (TTX) resistant. We investigated the impact of *SCN8A* alternative splicing on variant function by comparing the functional attributes of 15 variants expressed in 2 developmentally regulated splice isoforms (Na_V1.6N, Na_V1.6A). We employed automated patch clamp recording to enhance throughput, and developed a neuronal cell line (ND7/LoNav) with low levels of endogenous Na_V current to obviate the need for TTX-resistance mutations. Expression of Na_V1.6N or Na_V1.6A in ND7/LoNav cells generated Na_V currents with small, but significant, differences in voltage dependence of activation and inactivation. TTX-resistant versions of both isoforms exhibited significant functional differences compared with the corresponding WT channels. We demonstrated that many of the 15 disease-associated variants studied exhibited isoform-dependent functional effects, and that many of the studied *SCN8A* variants exhibited functional properties that were not easily classified as either gain- or loss-of-function. Our work illustrates the value of considering molecular and cellular context when investigating *SCN8A* variants.

Introduction

Pathogenic variants in genes encoding voltage-gated sodium (Na_V) channels are frequently discovered in individuals with early-onset epilepsy, developmental and epileptic encephalopathy (DEE), and related neurodevelopmental disorders (NDDs) (1, 2). Determining the functional consequences of Na_V channel variants can provide information about pathophysiological mechanisms and potentially guide precise therapeutic approaches (3, 4). Using the correct molecular context (e.g., species origin, splice isoform) for investigating function of an ion channel variant is vital for an accurate assessment.

Pathogenic variants in *SCN8A*, which encodes Na_V1.6, have emerged as important causes of neurodevelopmental disorders, with typical onset during infancy (5). The earliest discoveries associated DEE with nontruncating variants having gain-of-function properties (e.g., enhanced persistent current, altered voltage dependence of activation). Subsequently, *SCN8A* variants were discovered in individuals affected with epilepsy having a wider spectrum of clinical severity as well as NDD without seizures (6).

In mature neurons, Na_V1.6 is localized to the axon initial segment where the channel serves to initiate action potentials (7). The gene undergoes specific alternative splicing events during early development, including the in-frame inclusion of 1 of 2 distinct versions of exon 5 that encodes a portion of the first voltage-sensing domain (8). Exon 5N dominates during embryonic development and immediately after birth, but around 1 year of age transcripts containing the alternative exon 5A surpass those containing 5N, and the 5A isoform becomes predominant in later childhood through adulthood (9). Importantly, the *SCN8A* reference coding sequence designated as variant 1 (NM_014191) by the National Center for Biotechnology Information (NCBI) includes exon 5N, whereas the sequence including exon 5A is curated as

Conflict of interest: ALG received research grant funding from Praxis Precision Medicines, Neurocrine Biosciences, and Biohaven Pharmaceuticals, and is a member of the Scientific Advisory Board for Tevard Biosciences.

Submitted: November 10, 2023
Accepted: May 15, 2024
Published: May 21, 2024

Reference information: *JCI Insight*. 2024;9(12):e177530. https://doi.org/10.1172/jci.insight.177530.

variant 3 (NM_001330260). These annotations guided the early annotation of *SCN8A* variants by genetic testing laboratories such that pathogenic variants in exon 5A were initially overlooked (10).

Previous studies of *SCN8A* variant function used a variety of expression systems, including rodent Na_V1.6 (11–13) or the human channel with exon 5N (neonatal splice isoform) (14–19), which does not represent the most abundant splice isoform present during most of childhood and older (9). In some of these studies, Na_V1.6 was expressed in a neuronal cell line (ND7/23) that exhibits large endogenous sodium currents. To discriminate between the endogenous and heterologously expressed Na_V channels in these cells, many investigators exploited pore domain mutations of tyrosine-371 (Y371C or Y371S) to render Na_V1.6 insensitive to tetrodotoxin (TTX) (11–13, 16–21). However, this strategy could conceivably alter the functional impact of disease-associated variants, especially those located near the TTX interaction site in the channel structure. The heterogeneity in experimental approaches and recombinant Na_V1.6 channel constructs limits the comparisons of variant dysfunction across laboratories. A uniform experimental approach free from the potential confounds of endogenous currents and second-site mutations that also considers the most relevant splice isoform would be valuable.

In this study, we analyzed a series of *SCN8A* variants using automated patch clamp recording of recombinant human Na_V1.6 heterologously expressed in a derivative of ND7/23 neuronal cells that have low levels of endogenous Na_V current. We compared the functional properties of variants in the 2 isoforms generated by alternative splicing of exon 5 and used the relevant splice isoform to study a subset of variants discovered within exon 5A. Finally, we illustrate the importance of controlling for splice isoform by the functional study of an epilepsy-associated *SCN8A* haplotype with 2 de novo missense variants of uncertain significance within or outside exon 5N. Our findings demonstrate the importance of considering molecular and cellular context when investigating the functional consequences of *SCN8A* variants.

Results

We initially expressed recombinant WT human Na_V1.6 in HEK293T cells to evaluate efficiency and fidelity of automated patch clamp as a platform for evaluating the functional consequences of *SCN8A* variants. Results from these initial trials proved unsatisfactory because of inconsistent cell capture and suboptimal membrane seal formation. Therefore, we explored alternative cell lines, including the rat dorsal root ganglion neuron/mouse neuroblastoma hybrid ND7/23 cell line (22), which was used successfully by other groups for studying Na_V1.6 variants (11–13, 16–19, 21). Because ND7/23 cells exhibit a large endogenous fast-gating Na_V current, previous studies utilized a TTX-resistant mutant form of Na_V1.6 coupled with recording in the presence of TTX to isolate activity of the transfected channel. We chose an alternative approach designed to eliminate endogenous Na_V currents in ND7/23 cells, which obviates the need for TTX and non-native Na_V1.6 sequences that could confound analysis of disease-associated mutations.

Generation of a neuronal cell line with minimal Na_V current. Previously reported transcriptome analyses (23, 24) and pharmacological studies (25) deduced that Na_V1.7 was responsible for most of the endogenous Na_V current in ND7/23 cells. As additional proof, we transfected ND7/23 cells with siRNA targeting conserved sequences shared by rat and mouse Na_V1.7, and then assessed knockdown success by immunoblotting and manual patch clamp recording. Transient knockdown of Na_V1.7 eliminated immunodetectable protein and lowered endogenous Na_V current substantially (Figure 1, A and B). In separate experiments, we did not detect Na_V1.6 protein in ND7/23 cell lysates using 2 different polyclonal antibodies validated against mouse brain (Supplemental Figure 1; supplemental material available online with this article; https://doi.org/10.1172/jci.insight.177530DS1), indicating that the low level of *Scn8a* mRNA detected in ND7/23 cells (23, 24) likely does not contribute to functional Na_V channel expression.

For stable suppression of endogenous Na_V current in ND7/23 cells, we employed CRISPR/Cas9 genome editing to disrupt the coding sequences of rat and mouse Na_V1.7 (see Methods). An initial round of gene editing yielded clonal lines with multiple frame-shifting deletions in both rat and mouse Na_V1.7, but a small subpopulation of channel sequences with in-frame deletions was also observed. A second round of gene editing was successful in introducing frame shifts in all detectable Na_V1.7 transcripts. Two clones with negligible endogenous Na_V1.7 protein levels (Figure 1C) and small endogenous inward currents (peak current density less than 15 pA/pF; Figure 2, A and B) were selected. The final clonal cell line (designated ND7/LoNav) was efficiently electroporated with human Na_V1.6 and proved amenable to high-throughput automated patch clamp analysis. We did not observe overt differences in cell morphology between original and derivative cell lines.

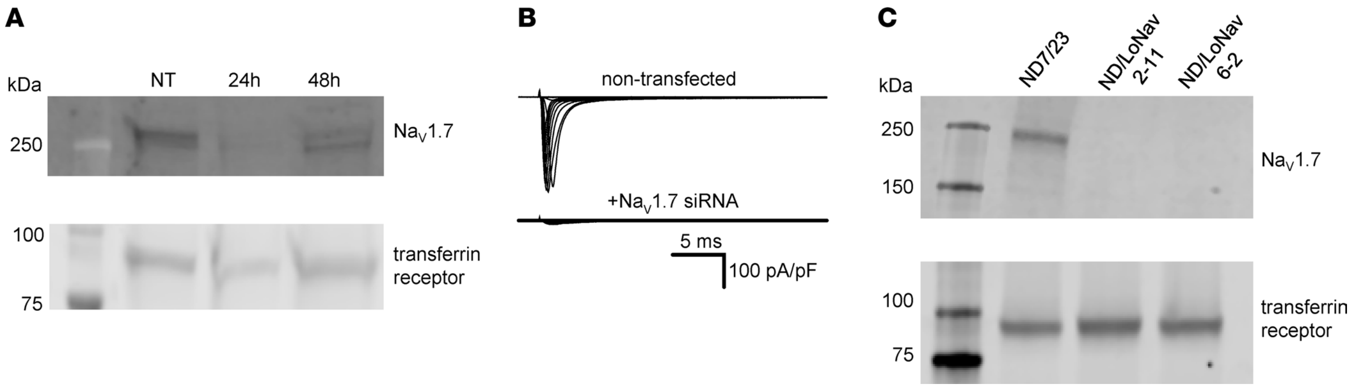

Figure 1. Na$_V$1.7 siRNA reduces whole-cell current and Na$_V$1.7 protein expression in ND7/23 cells. (**A**) Immunoblots of Na$_V$1.7 and transferrin receptor (loading control) isolated from nontransfected (NT) and Na$_V$1.7 siRNA–transfected (24 and 48 hours after transfection) ND7/23 cells. (**B**) Average whole-cell currents from nontransfected (n = 3) and Na$_V$1.7 siRNA–transfected (n = 4) ND7/23 cells recorded by manual patch clamp. (**C**) Immunoblots of Na$_V$1.7 and transferrin receptor isolated from ND7/23 and 2 clonal ND7/LoNav cell lines.

Na$_V$1.6 splice isoforms exhibit distinct functional properties. We compared the functional properties of adult (Na$_V$1.6A) and neonatal (Na$_V$1.6N) splice isoforms expressed in ND7/LoNav cells. Cells expressing either Na$_V$1.6A or Na$_V$1.6N exhibited large, voltage-activated inward currents with similar peak current densities, which were approximately 6-fold larger and had distinct biophysical properties compared with currents recorded from nontransfected cells (Figure 2, A and B, and Supplemental Data Set 1). Cells expressing either Na$_V$1.6 isoform generated whole-cell currents with similar inactivation kinetics; however, there were small but significant differences between Na$_V$1.6A and Na$_V$1.6N in the voltage dependence of activation (Supplemental Data Set 1). Specifically, Na$_V$1.6A exhibited a hyperpolarized $V_{1/2}$ (difference of –2.9 ± 0.5 mV) and steeper voltage dependence of activation (Figure 2C) along with a hyperpolarized voltage dependence of inactivation ($V_{1/2}$ difference of –3.4 ± 0.4 mV) (Figure 2D) relative to Na$_V$1.6N. These results indicate that Na$_V$1.6A and Na$_V$1.6N exhibit distinct biophysical properties, and suggest that the functional consequences of disease-associated Na$_V$1.6 variants may be influenced by the splice isoform.

Functional consequences of disease-associated SCN8A variants. We determined the functional properties of 8 disease-associated *SCN8A* missense variants (Q417P, R850Q, G1475R, R1617L, G1625R, I1631M, N1768D, and N1877S) and 2 ultrarare variants of uncertain significance reported in the ClinVar database (https://www.ncbi.nlm.nih.gov/clinvar/) (Q713D and G1914S) in both Na$_V$1.6A and Na$_V$1.6N. Five variants (R850Q, G1475R, R1617L, G1625R, and N1877S) are recurrent, and 3 (R850Q, G1475R, and R1617L) were previously investigated to determine mutation-associated functional effects (13, 15–17, 26). Three nonrecurrent variants were Q417P, which was found in a female with intractable infantile spasms and global developmental delay (also reported in ref. 27), I1631M discovered in a male with generalized epilepsy with onset at age 5 months followed in later childhood by partial epilepsy and mild intellectual disability, and N1768D (11). We investigated the functional consequences of 3 other disease-associated variants discovered in exon 5A (V211R, R223G, and I231T) (10) only in Na$_V$1.6A. A summary of clinical phenotypes associated with each variant is presented in Supplemental Table 1. We also investigated the functional properties of 2 engineered TTX-resistance mutations (Y371C and Y371S) in both Na$_V$1.6A and Na$_V$1.6N. The location of all studied variants on the Na$_V$1.6 protein are illustrated in Supplemental Figure 2. For this study, we analyzed electrophysiological data from 3,884 cells.

Variant-specific effects on channel properties were determined by quantifying differences relative to isoform-matched WT channels that were expressed and recorded in parallel. We analyzed current density, time constant (τ) of fast inactivation at 0 mV, voltage dependence of activation and inactivation, window current, frequency-dependent loss of channel availability (i.e., current rundown measured at 20 Hz), recovery from fast inactivation, persistent current, and net charge movement during slow voltage ramps. Averaged whole-cell currents normalized to peak isoform-matched WT current are presented in Supplemental Figures 3 and 4 for variants expressed in Na$_V$1.6N and Na$_V$1.6A, respectively.

Cells expressing most variants exhibited robust current, with the exception of R1617L expressed in the Na$_V$1.6N splice isoform (Supplemental Data Sets 2 and 3). Measurable current density was significantly smaller than isoform-matched WT for 3 variants in the adult isoform and 7 in the neonatal isoform.

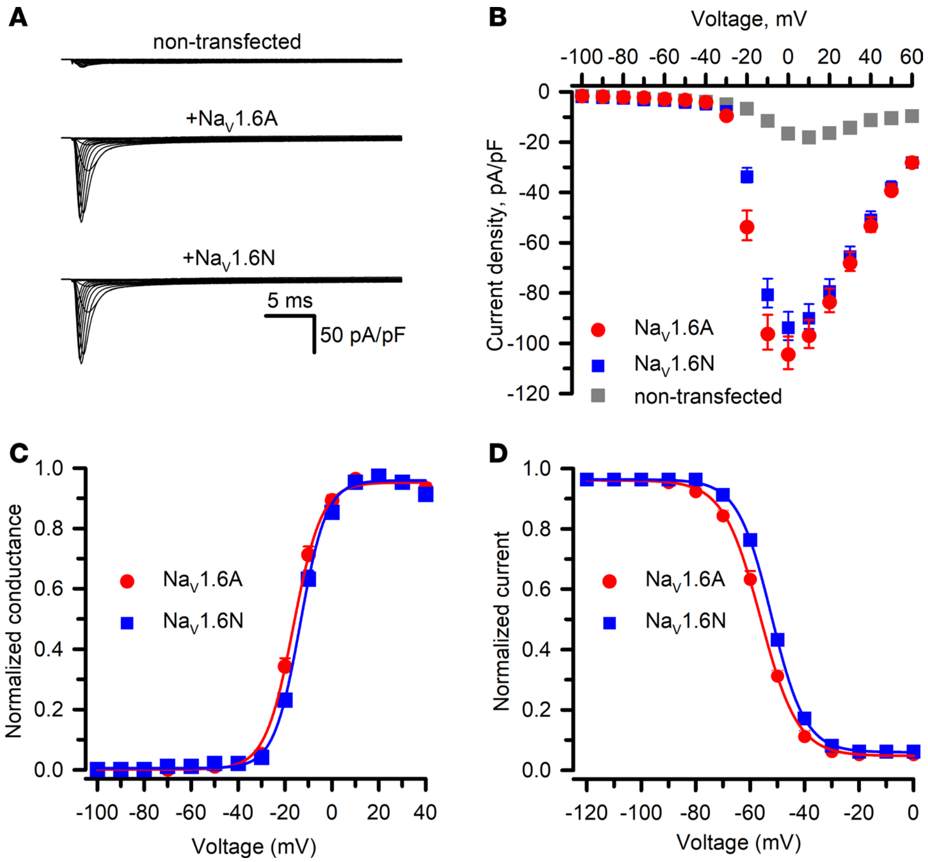

Figure 2. Functional properties of Na$_V$1.6N and Na$_V$1.6A expressed in ND7/LoNav cells. (**A**) Average whole-cell currents recorded using automated patch clamp from nontransfected ND7/LoNav cells or transiently transfected with Na$_V$1.6A or Na$_V$1.6N. In these experiments, transfection efficiency of WT Na$_V$1.6A and Na$_V$1.6N averaged 78.3% ± 3.5% and 74.4% ± 5.1%, respectively, and approximately 65% of wells in each 384-well plate exhibited cell capture and formation of stable high resistance (≥0.5 GΩ) membrane seals. (**B**) Average current density versus voltage measured from nontransfected ND7/LoNav cells (gray squares, $n = 103$), Na$_V$1.6A (red circles, $n = 90$), or Na$_V$1.6N (blue squares, $n = 86$). (**C**) Conductance-voltage plots recorded from ND7/LoNav cells expressing Na$_V$1.6A (red circles, $n = 96$) or Na$_V$1.6N (blue squares, $n = 90$). (**D**) Voltage dependence of inactivation recorded from ND7/LoNav cells expressing Na$_V$1.6A (red circles, $n = 139$) or Na$_V$1.6N (blue squares, $n = 142$). Quantitative data with statistical comparisons are provided in Supplemental Data Set 1.

Only 1 variant (G1475R) exhibited larger current density (Figure 3), and the increase was similar in both isoforms. Activation-voltage dependence varied considerably among this cohort of variants, with some exhibiting significantly depolarized or significantly hyperpolarized conductance-voltage relationships (Figure 4). Similarly, the voltage dependence of inactivation was significantly depolarized, significantly hyperpolarized, or WT-like (Figure 5). The overlap between the activation and inactivation curves illustrated in Figure 4B and Figure 5B, respectively, can be quantified as window current (Supplemental Figure 5), which defines a voltage range in which channels are activated but not inactivated. Most variants exhibited a significantly larger window current consistent with gain of function, whereas only 1 variant (I231T) had a significantly smaller window current.

Inactivation kinetics (measured at 0 mV), persistent current, and ramp current amplitudes were also variable, with notable slowing of inactivation time course and greater persistent or ramp current for multiple variants (Figure 6 and Figure 7), which are consistent with gain of function. Only R223G exhibited smaller persistent or ramp current than WT. Persistent current was most prominent for the epilepsy-associated variant N1768D, in agreement with previous reports (11, 14). The kinetics observed for recovery from inactivation (Supplemental Figure 6) and frequency-dependent current rundown (Supplemental Figure 7) illustrate differences for some variants that are consistent with loss of function. The variants with the slowest recovery from inactivation were N1768D and Q417P expressed in either Na$_V$1.6N or Na$_V$1.6A, and this correlated with variable degrees (5%–13%) of frequency-dependent current rundown measured at 20 Hz.

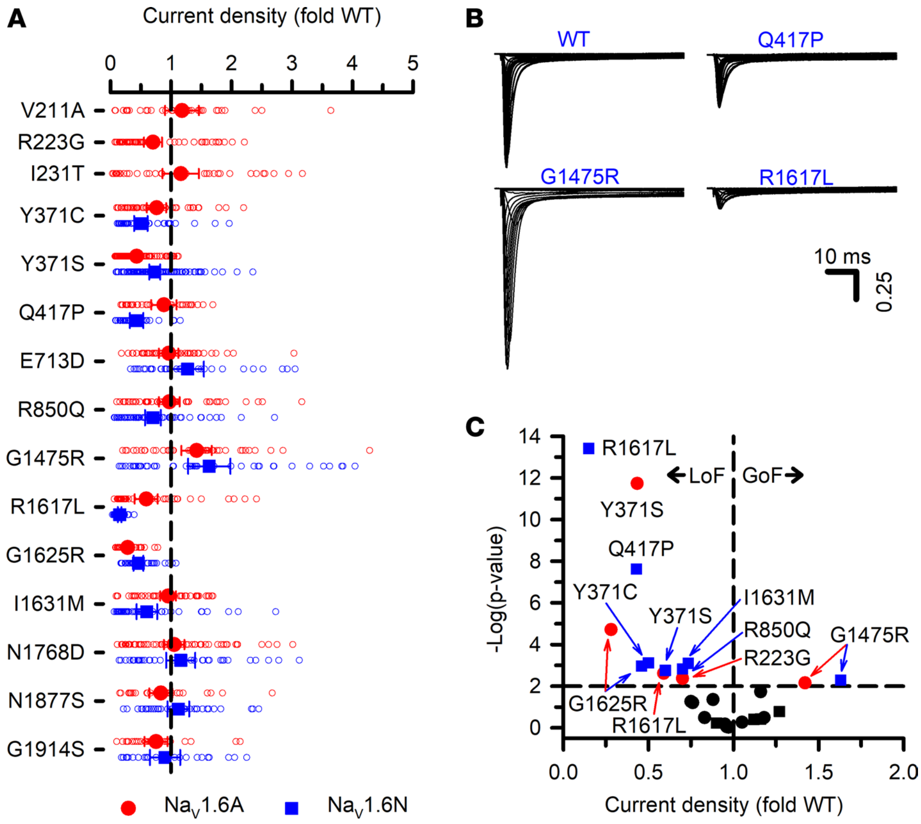

Figure 3. Current density of Na$_V$1.6 variants. (**A**) Peak whole-cell current density for Na$_V$1.6 variants displayed as fold difference from WT channels recorded in parallel. All individual data points are plotted as open symbols and mean values are shown as larger filled symbols (n = 35–108 per variant). Error bars represent 95% CI. Data from Na$_V$1.6A or Na$_V$1.6N are indicated as red or blue symbols, respectively. Values to the right or left of the vertical dashed line (normalized WT value) represent current density larger or smaller than WT, respectively. (**B**) Averaged current traces, normalized to WT peak current density, for WT Na$_V$1.6N and select variants with either larger (G1475R) or smaller (Q417P) current density. (**C**) Volcano plot of mean values highlighting variants with peak current density significantly ($P < 0.01$, horizontal dashed line) different from WT. Symbols to the left of the vertical dashed line denote smaller current (loss of function, LoF), while symbols to the right indicate larger current (gain of function, GoF). Black symbols represent variants with no significant difference from WT. Quantitative data with statistical comparisons are provided in Supplemental Data Set 2 (Na$_V$1.6N) and Supplemental Data Set 3 (Na$_V$1.6A).

Our investigation of the functional consequences of *SCN8A* using the 2 alternatively spliced versions of the channel revealed several variants with significant isoform-dependent properties. For a given variant, the magnitude of difference compared with the isoform-matched WT channel can be greater in either Na$_V$1.6N or Na$_V$1.6A (summarized in radar plots, Supplemental Figure 8). For example, the recurrent variant G1625R exhibits a greater degree of inactivation slowing and larger shifts in activation and inactivation $V_{1/2}$ in Na$_V$1.6A, whereas the degree of dysfunction was less severe in the neonatal isoform.

Our results demonstrated that disease-associated Na$_V$1.6 variants exhibited various biophysical defects consistent with either gain of function (e.g., slower and less complete inactivation, hyperpolarized voltage dependence of inactivation) or loss of function (depolarized voltage dependence of activation, slower recovery from inactivation). However, opposing functional properties were observed for specific variants and this confounded the assignment of an overall effect using a simple binary classification scheme. We summarized the functional properties assessed for each variant expressed in either Na$_V$1.6N or Na$_V$1.6A in Supplemental Table 2, and generated heatmaps that scaled each measured parameter along a functional axis from loss to gain (Supplemental Figure 9). The heatmaps illustrate that most of the Na$_V$1.6 variants exhibit complex patterns of dysfunction, a pattern also observed for *SCN2A* (Na$_V$1.2) variants (28). The 2 *SCN8A* variants of uncertain significance (Q713D and G1914S) we studied exhibited minimal to no functional perturbations.

Functional effects of a TTX-resistant variant. An advantage of using ND7/LoNav cells is the ability to express a Na$_V$ channel in a neuronal cell environment without requiring a pharmacological strategy to

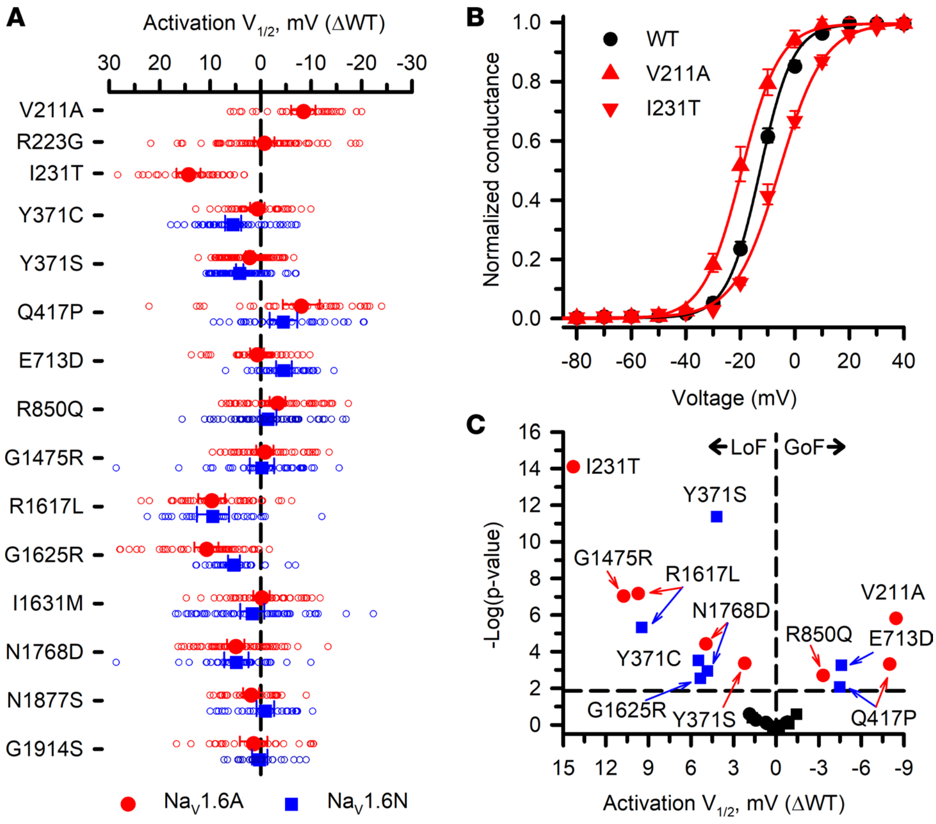

Figure 4. Voltage dependence of activation for Na$_V$1.6 variants. (**A**) Averaged voltage dependence of activation V$_{1/2}$ obtained from fitting the data for each variant-expressing cell and plotted as difference (ΔV$_{1/2}$ in mV) from the averaged V$_{1/2}$ for WT channels recorded in parallel. All individual data points are plotted as open symbols and mean values are shown as larger filled symbols (*n* = 22–77 per variant). Error bars represent 95% CI. Data from Na$_V$1.6A or Na$_V$1.6N are indicated as red or blue symbols, respectively. Values to the right or left of the vertical dashed line (no difference from WT) indicate hyperpolarized (gain of function) or depolarized (loss of function) activation V$_{1/2}$, respectively. (**B**) Conductance-voltage relationships for select variants expressed in Na$_V$1.6A (red lines) illustrating hyperpolarized (V211A) or depolarized (I231T) shifts in activation V$_{1/2}$ relative to WT channels (black line) recorded in parallel. (**C**) Volcano plot of mean values highlighting variants with significantly different ($P < 0.01$, horizontal dashed line) activation V$_{1/2}$. Symbols to the left of the vertical dashed line denote depolarized V$_{1/2}$ values (loss of function, LoF), while symbols to the right indicate hyperpolarized V$_{1/2}$ values (gain of function, GoF). Black symbols represent variants with no significant difference from WT. Quantitative data with statistical comparisons are provided in Supplemental Data Set 2 (Na$_V$1.6N) and Supplemental Data Set 3 (Na$_V$1.6A).

negate endogenous current. Because engineering TTX resistance has been widely used to distinguish Na$_V$1.6 current from endogenous Na$_V$ current in the original ND7/23 cell line, we examined functional properties of 2 TTX-resistant variants, Y371C and Y371S (11–13, 16–21) expressed in ND7/LoNav cells. Expression of Y371C or Y371S gave rise to measurable voltage-dependent Na$_V$ currents in both Na$_V$1.6N and Na$_V$1.6A, but there were significant and heterogeneous differences in functional properties compared with cells expressing the isoform-matched WT channel. Current density was significantly smaller and the voltage dependence of activation was significantly depolarized for Y371S in both isoforms and for Y371C in Na$_V$1.6A only (Figures 3 and 4). Recovery from inactivation was significantly slower for both Na$_V$1.6N-Y371C and Na$_V$1.6N-Y371S, but was WT-like for Na$_V$1.6A-Y371S and significantly faster for Na$_V$1.6A-Y371C (Supplemental Figure 6). The voltage dependence of inactivation was significantly depolarized only for Na$_V$1.6A-Y371C (Figure 5). We also observed significant differences in inactivation kinetics between isoform-matched WT channels and cells expressing either TTX-resistant variant (Figure 6). Our findings indicated that TTX-resistant variants of Y371 affect the function of Na$_V$1.6 in our experimental system.

Value of studying variants in Na$_V$1.6 splice isoforms. To further emphasize the importance of studying disease-associated variants in the most relevant Na$_V$1.6 splice isoform, we demonstrated the functional consequences of a complex *SCN8A* genotype discovered in a female infant with early-onset DEE. The affected individual exhibited focal seizures and infantile spasms beginning at age 3 months, which

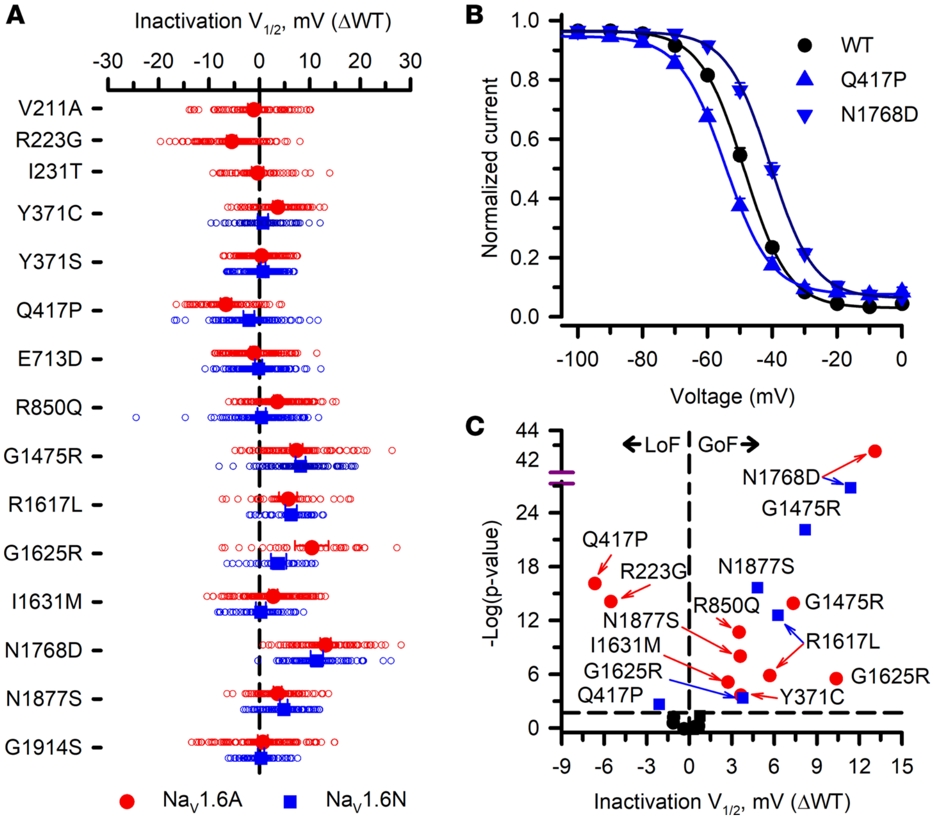

Figure 5. Voltage dependence of inactivation for Na$_V$1.6 variants. (**A**) Averaged voltage dependence of inactivation V$_{1/2}$ obtained from fitting the data for each variant-expressing cell and plotted as difference (ΔV$_{1/2}$ in mV) from the averaged V$_{1/2}$ for WT channels recorded in parallel. All individual data points are plotted as open symbols and mean values are shown as larger filled symbols (*n* = 29–142 per variant). Error bars represent 95% CI. Data from Na$_V$1.6A or Na$_V$1.6N are indicated as red or blue symbols, respectively. Values to the right or left of the vertical dashed line (no difference from WT) indicate depolarized (gain of function) or hyperpolarized (loss of function) inactivation V$_{1/2}$, respectively. (**B**) Steady-state inactivation curves for select variants expressed in Na$_V$1.6N (blue lines) illustrating hyperpolarized (Q417P) or depolarized (N1768D) inactivation V$_{1/2}$ relative to WT channels (black line) recorded in parallel. (**C**) Volcano plot of mean values highlighting variants with significantly different ($P < 0.01$, horizontal dashed line) inactivation V$_{1/2}$. Symbols to the left of the vertical dashed line denote hyperpolarized V$_{1/2}$ values (loss of function, LoF), while symbols to the right indicate depolarized V$_{1/2}$ values (gain of function, GoF). Black symbols represent variants with no significant difference from WT. Quantitative data with statistical comparisons are provided in Supplemental Data Set 2 (Na$_V$1.6N) and Supplemental Data Set 3 (Na$_V$1.6A).

were largely refractory to multiple drug treatments. She later developed tonic seizures, hypotonia, and cortical visual impairment. Clinical genetic testing identified 2 de novo missense variants (c.431C>G, p.T144S; c.649T>C, p.S217P). Subsequent long-read genomic sequence analysis identified a third synonymous variant (c.660C>G, p.R220R) and demonstrated that all 3 variants were present in the same *SCN8A* allele. Importantly, both S217P and R220R are located within exon 5N, whereas T144S was in a neighboring exon not subject to alternative splicing. Because of the presumed developmentally regulated exclusion of exon 5N and uncertainty about which variant was pathogenic, we investigated the functional properties of the compound T144S/S217P/R220R genotype in neonatal Na$_V$1.6N, and the single T144S variant in the Na$_V$1.6A isoform (Figure 8).

Compared with the WT channel, the triple variant in Na$_V$1.6N exhibited significantly smaller whole-cell currents, significantly hyperpolarized shifts in the voltage dependence of activation and inactivation, slower recovery from inactivation, and larger persistent and ramp currents (Figure 8, A–C, and Supplemental Data Set 2). By contrast, T144S expressed in the Na$_V$1.6A isoform exhibited mostly WT-like properties, with the exception of slightly slower inactivation kinetics and modestly larger ramp current and window current (Figure 8, D and E, and Supplemental Data Set 3). Although only the triple variant channel had altered voltage dependence of inactivation, both variants exhibited slower time course of inactivation measured at 0 mV, which was greater for the compound variant expressed in Na$_V$1.6N. We concluded that the

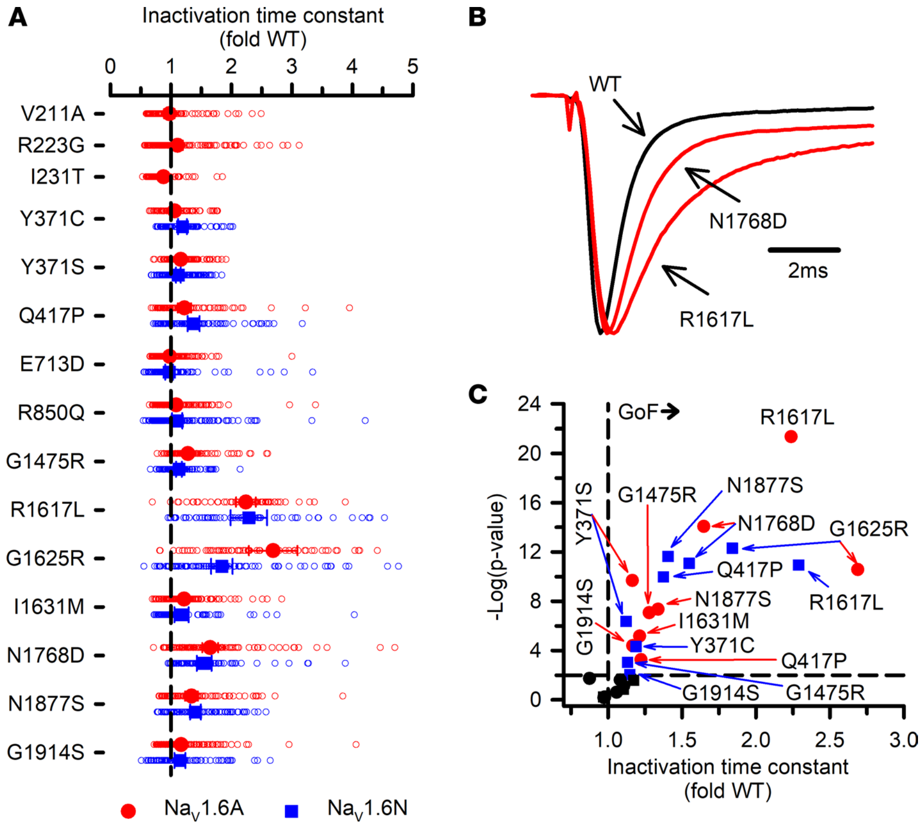

Figure 6. Inactivation kinetics for Na$_V$1.6 variants. (**A**) Averaged inactivation time constants measured at 0 mV obtained by fitting current decay for each variant cell with a single exponential function and expressed as a ratio to the averaged WT channel value recorded in parallel. All individual data points are plotted as open symbols and mean values are shown as larger filled symbols (*n* = 57–160 per variant). Error bars represent 95% CI. Data from Na$_V$1.6A or Na$_V$1.6N are indicated as red or blue symbols, respectively. Values to the right or left of the vertical dashed line (average normalized WT value) indicate slower (gain of function) or faster (loss of function) inactivation kinetics, respectively. (**B**) Averaged traces recorded at 0 mV, normalized to the peak current density for select variants illustrating faster (V211A) or slower (N1768D) inactivation. (**C**) Volcano plot of mean values highlighting variants with significantly different ($P < 0.01$, horizontal dashed line) inactivation time constants. Symbols to the right of the vertical dashed line represent slower inactivation kinetics (gain of function, GoF). No variants exhibited significantly faster inactivation. Black symbols represent variants with no significant difference from WT. Quantitative data with statistical comparisons are provided in Supplemental Data Set 2 (Na$_V$1.6N) and Supplemental Data Set 3 (Na$_V$1.6A).

triple variant channel in the neonatal splice isoform exhibits mixed dysfunctional properties that individually represented either loss of function (e.g., smaller current density, hyperpolarized voltage dependence of inactivation, slower recovery from inactivation) or gain of function (e.g., hyperpolarized activation voltage dependence, slower time course of fast inactivation, larger persistent and ramp currents) and is the likely pathogenic driver of the clinical phenotype. This also suggests that suppression of exon 5N incorporation into mature *SCN8A* mRNA transcripts may be a therapeutic strategy in this case.

Discussion

In this study, we demonstrated the importance of considering alternative splicing when assessing disease-associated *SCN8A* variants, and validated 2 experimental strategies for accomplishing this task (creation of a neuronal cell line with low endogenous sodium currents and use of automated patch clamp recording). In combination, these approaches provide the means for greater physiological relevance and higher throughput that will help standardize efforts to determine the functional consequences of *SCN8A* variants, which is important for assessing variant pathogenicity, ascertaining molecular pathogenesis, and for screening therapeutic agents (21). In particular, automated patch clamp recording is increasingly used to assess the functional consequences of human ion channel variants at a scale difficult to achieve with traditional electrophysiological methods (28–38).

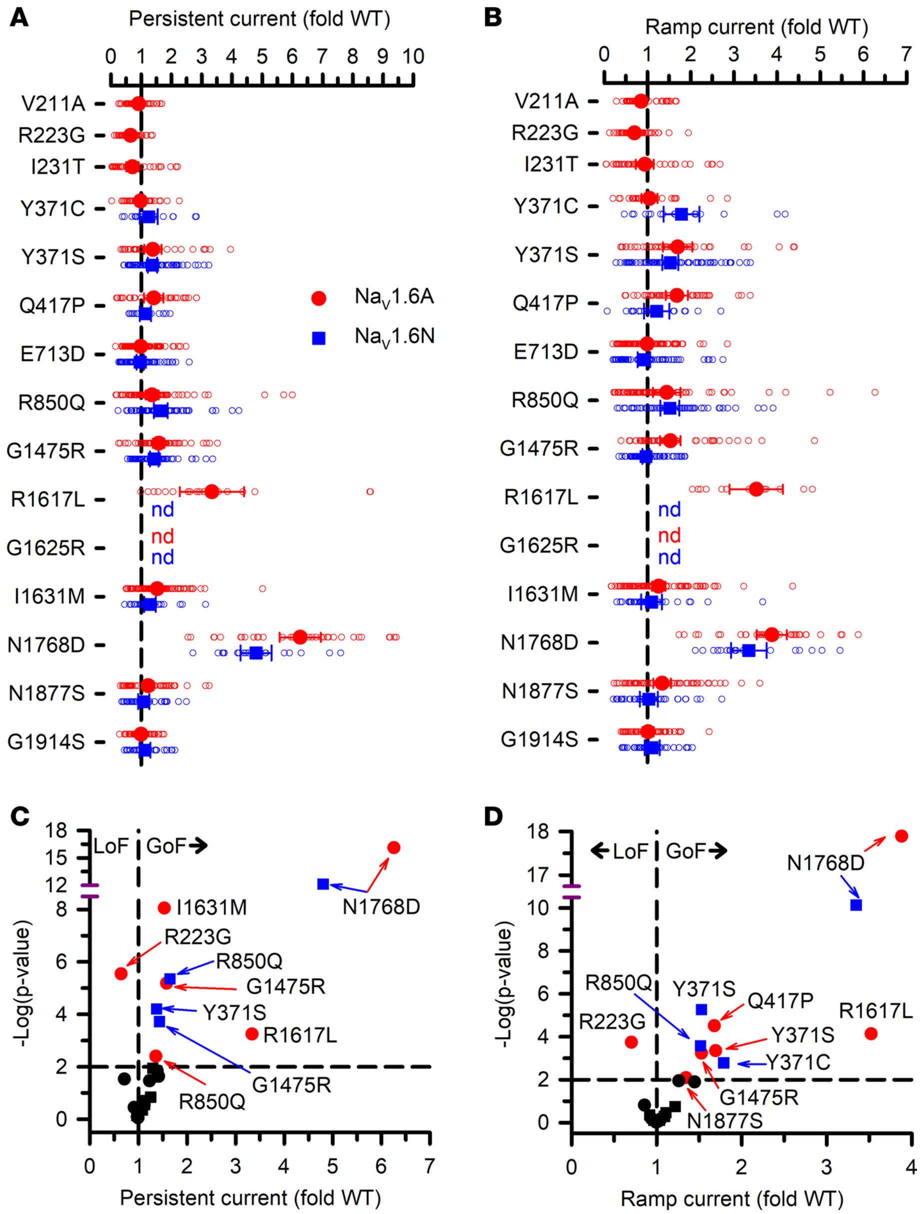

Figure 7. Persistent and ramp currents for $Na_V1.6$. (**A** and **B**) Average persistent current amplitude (**A**) or net charge movement during a depolarizing voltage ramp (**B**) for variants displayed as fold differences from WT channels recorded in parallel. All individual data points are plotted as open symbols and mean values are shown as larger filled symbols (*n* = 9–94 per variant). Values for some variants were not determined (nd) because whole-cell current density was too small. Error bars represent 95% CI. Data from $Na_V1.6A$ or $Na_V1.6N$ are indicated as red or blue symbols, respectively. Values to the right or left of the vertical dashed lines (average normalized WT values) indicate larger (gain of function) or smaller (loss of function) currents, respectively. (**C** and **D**) Volcano plots of mean values highlighting variants with significantly different ($P < 0.01$, horizontal dotted line) levels of persistent current (**C**) or ramp current (**D**) compared with WT channels. Symbols to the left of the vertical dashed lines denote smaller current levels (loss of function, LoF), while symbols to the right indicate larger current levels (gain of function, GoF). Black symbols represent variants with no significant difference from WT. Quantitative data with statistical comparisons are provided in Supplemental Data Set 2 ($Na_V1.6N$) and Supplemental Data Set 3 ($Na_V1.6A$).

A focus of our study was on comparing the functional properties of WT and variant $Na_V1.6$ expressed in 2 distinct splice isoforms of the channel ($Na_V1.6N$ and $Na_V1.6A$). Human brain Na_V channel genes undergo developmentally regulated alternative splicing, including a well-characterized event involving 2 distinct versions of the fifth coding exon that encode portions of the first voltage-sensing domain (8). Transcriptome profiling of human brain indicates that $Na_V1.6N$ is the most abundant *SCN8A* transcript before birth, whereas $Na_V1.6A$ becomes the major splice isoform by around age 1 year (9), with

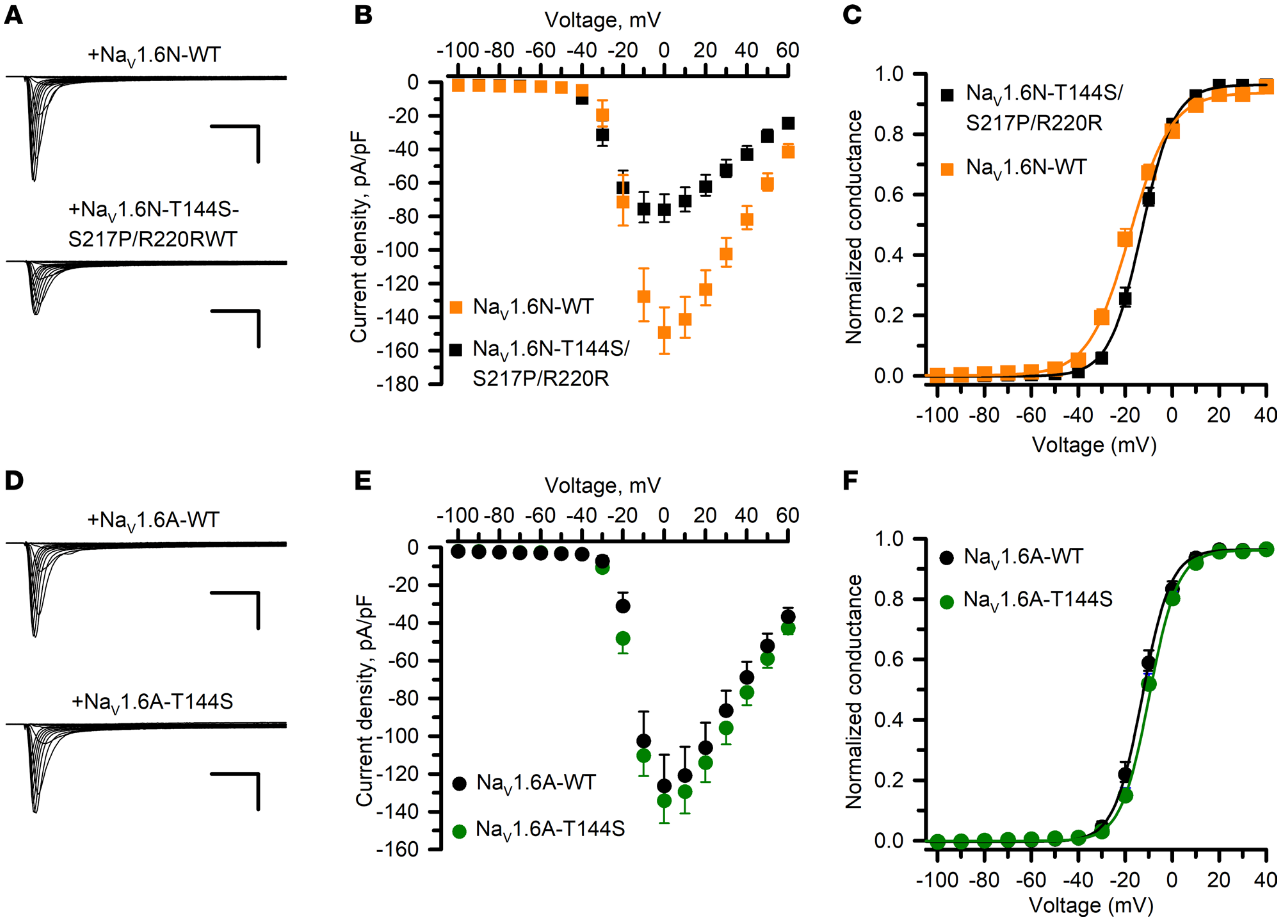

Figure 8. Functional properties of a complex *SCN8A* genotype of uncertain significance. (**A**) Averaged whole-cell current density recorded from ND7/LoNav cells expressing WT or variant Na$_V$1.6N channels (n = 71–78 per variant). Scale bars: 5 ms (horizontal) and 25 pA/pF (vertical). (**B**) Current-voltage plots comparing WT (black symbols and lines) and variant (orange symbols and lines) Na$_V$1.6N channels. Current amplitudes were normalized to cell capacitance to determine current density. (**C**) Conductance-voltage plots for WT (black symbols and lines) and variant (orange symbols and lines) Na$_V$1.6N channels. (**D**) Averaged whole-cell current density recorded from ND7/LoNav cells expressing WT or variant Na$_V$1.6A channels (n = 51–75 per variant). Scale bars: 5 ms (horizontal) and 50 pA/pF (vertical). (**E**) Current-voltage plots comparing WT (black symbols and lines) and variant (green symbols and lines) Na$_V$1.6A channels. Current amplitudes were normalized to cell capacitance to determine current density. (**F**) Conductance-voltage plots for WT (black symbols and lines) and variant (green symbols and lines) Na$_V$1.6A channels. Quantitative data with statistical comparisons are provided in Supplemental Data Set 2 (Na$_V$1.6N) and Supplemental Data Set 3 (Na$_V$1.6A). Error bars in panels **B**, **C**, **E**, and **F** represent 95% CI.

a transition sometime during infancy, but there is interindividual variability in the timing of this event and it is not known how pathogenic *SCN8A* variants affect alternative splicing.

At the typical age of onset of neurological symptoms in *SCN8A*-related disorders (4–6 months), there is a mix of splice isoforms containing either exon 5A or 5N (9). Published studies on the functional consequences of *SCN8A* variants only use cDNA constructs representing rodent Na$_V$1.6 (splice isoform unclear) (11–13) or the neonatal splice isoform of the human channel (14–19, 39). It is conceivable that pathogenic *SCN8A* variants disrupt the timing of alternative splicing in one direction or the other. Our study considered both splice isoforms to ensure we captured the most physiologically relevant molecular context, and determined that the functional properties for some variants are isoform dependent.

SCN8A exons 5N and 5A encode proteins that differ by 2 amino acids at positions 207 (5A: isoleucine; 5A: valine) and 212 (5N: asparagine; 5A: aspartate), and these differences are sufficient to affect the functional properties of the respective channel splice isoforms (Figure 2 and Supplemental Data Set 1). The neurophysiological consequences of this alternative splicing event for *SCN8A* in vivo are unknown, but the analogous splicing event in mouse Na$_V$1.2 correlates with greater cortical pyramidal neuron excitability beginning after postnatal day 3 that persists into adulthood (40) and a computational model of a human cortical pyramidal neuron exhibits higher firing frequency when Na$_V$1.2A is incorporated (41). Based on our electrophysiological observations, Na$_V$1.6N exhibits slightly depolarized voltage dependence of both activation and inactivation that have the potential of affecting neuronal excitability. Prior studies suggested that shifts in $Na_V1.6$ activation voltage dependence have a greater impact on neuronal firing than similar shifts in the voltage dependence of inactivation (16), and we could speculate that $Na_V1.6N$ expression renders immature neurons less excitable.

Because we considered the molecular context for *SCN8A* variants to be relevant to understanding their functional consequences, we investigated the functional properties of variants located exclusively in either exon 5A or 5N using the relevant splice isoform. One variant (R223G) was previously studied in a TTX-resistant version of human $Na_V1.6N$ expressed in ND7/23 cells (20), and findings from that study differ from our data on human $Na_V1.6A$-R223G expressed in ND7/LoNav cells (20). Specifically, the previous study demonstrated hyperpolarized activation voltage dependence and faster recovery from inactivation, whereas our data indicated WT-like activation voltage dependence, and slower recovery from inactivation. Two other variants (R850Q and G1475R) previously studied in TTX-resistant $Na_V1.6N$ also exhibited functional differences with our study using the human $Na_V1.6A$ isoform. The previous work on R850Q highlighted large persistent current and hyperpolarized voltage dependence of activation (17), which we also observed, but our findings differed in the impact on inactivation voltage dependence and recovery from inactivation. Similarly, prior work on G1475R in human TTX-resistant $Na_V1.6N$ (16, 18) differed from our work with $Na_V1.6A$ in current density, persistent current, and ramp current. A recent study of G1625R performed in mouse Neuro-2a cells using human TTX-resistant $Na_V1.6N$ reported qualitatively similar, but quantitatively different, findings compared with our results (39). Not all variants, including variants N1768D and G1625R, exhibit isoform-dependent properties. A summary of differences between our study and previously reported work is presented in Supplemental Table 3.

The value of studying variants in the correct molecular context was also illustrated by our investigation of a complex genotype with 3 in-phase variants of uncertain significance discovered in an infant with severe DEE. This work allowed us to demonstrate which genotype was most likely to be pathogenic, and provided data supporting the potential therapeutic value of induced exon 5 splice switching (42).

In addition to considering the relevant splice isoform, we also developed a cellular platform for investigating *SCN8A* variants that exploits a neuronal cell environment without requiring a pharmacological intervention to isolate human $Na_V1.6$ current. We developed ND7-LoNav cells by genetically inactivating endogenous rodent $Na_V1.7$, resulting in a neuron-derived cell line without appreciable background sodium current. While this cell line has value for studying brain Na_V channel variants in vitro, it is important to point out that these cells are not human and were not derived from central neurons. Separate studies in native neurons may have additional value in relating the functional effects of variants to neuronal physiology.

Use of LoNav cells obviates the need for a second site mutation to render human $Na_V1.6$ TTX resistant (14, 16–19). Our approach avoids the potential confounding effects of TTX-resistance mutations at amino acid position 371 (Y371C and Y371S), which we demonstrated have significant functional differences from WT channels in either $Na_V1.6N$ or $Na_V1.6A$. Other studies have shown that a corresponding TTX-resistance mutation in $Na_V1.3$ (Y384S) also exhibits dysfunctional properties (43). We raise concern that some prior findings may be confounded by extra pore domain mutations.

One goal of determining the functional consequences of *SCN8A* variants is to aid in building genotype-phenotype correlations. Such correlations are valuable for understanding differences in pathophysiological mechanisms and may help guide pharmacological therapy such as the use of Na_V channel–blocking antiseizure medications, which would be most useful in the setting of gain-of-function variants. The majority of variants we studied exhibited multiple functional disturbances that individually are consistent with either gain or loss of function, but the net effect of these effects can be challenging to determine without additional experimental work. For some variants such as N1768D, enhanced persistent current combined with depolarized voltage dependence of inactivation are likely drivers of elevated seizure susceptibility. However, even this widely accepted gain-of-function variant exhibits other functional properties that are consistent with loss of function, including depolarized voltage dependence of activation (Figure 4), slower recovery from inactivation (Supplemental Figure 6), and a greater tendency for frequency-dependent loss of activity (Supplemental Figure 7). Of note, we did not interrogate resurgent current in our study, but previous studies suggested that this biophysical feature can be affected by certain *SCN8A* variants (14, 17). Complementary experimental approaches with computational simulation of neuronal action potentials (44) or dynamic action potential clamp (45, 46) may be valuable next steps.

In summary, we standardized an approach for evaluating the functional consequences of *SCN8A* variants that exploits the higher throughput achievable with automated patch clamp recording and obviates the need for second-site TTX-resistance mutations through use of a neuronal cell line with low levels of endogenous Na_V current. Our findings demonstrate that developmentally regulated alternative splicing of exon 5 influences variant function and emphasize the importance of studying variants in physiologically relevant splice isoforms.

Methods

Sex as a biological variable. Our study indirectly involved deidentified human participants who have a rare disorder. Sex was not declared for all participants. We were not powered to address sex as a biological variable.

Long-read SCN8A genomic sequencing. Cheek swab genomic DNA was obtained from a proband carrying 2 de novo *SCN8A* missense variants and from both parents. To determine the phase of the 2 variants in the proband, long-range genomic PCR was performed under dilute conditions with long extension times and Phusion High Fidelity Polymerase (Thermo Fisher Scientific) using primers targeting an amplicon of approximately 2.6 kb encompassing both variants (forward: CTCTTCTGTGCTTCACCTTTCTCTAGC; reverse: CCTATCCCAACACCTAACACCAACC). Samples were analyzed for quantity and quality using UV-Vis spectrometry and Femto Pulse (Agilent) pulsed-field capillary electrophoresis, followed by standard SMRTbell PacBio (Pacific Biosciences) library preparation. Library quality control was done using Qubit fluorometric analysis (Thermo Fisher Scientific).

Long-read sequencing of the 3 libraries was performed using a single flow cell on a PacBio Sequel v3r9 (Pacific Biosciences) at the Massachusetts Institute of Technology Biomicro Center using PacBio Circular Consensus Sequencing to improve base-calling accuracy. Sequence reads from the proband sample were first filtered for lengths in the 2500–2700 bp range. Sequences were then filtered for the presence of four 21-bp "anchor" segments (A, B, C, and D) arranged AV_1B to CV_2D. Anchor segments were defined as 21-bp reference genomic sequences located immediately upstream or downstream of each variant (V_1, V_2), with no filter on the identity of the base at the V_1 or V_2 position. After discovery of a third synonymous variant (V_3) described below, the filter for the D anchor was adjusted to allow any base at the location of V_3 in this anchor. This filtering yielded 73,522 sequences. Sequences were scored for the presence of the variant (V) or reference (R) allele at the V_1 or V_2 position, yielding 46% V/V, 40% R/R, 7% V/R, and 7% R/V sequences, indicating a relatively low representation of chimeric products, and indicating that the 2 variants are in *cis*. Similar analyses of the parental samples yielded approximately 99% reference allele at both variant positions, confirming that both variants arose de novo in the proband. Visual inspection of multiple sequence alignments of proband amplicon sequences also revealed the presence of V_3 — g.52082587C>G (chr12, hg19) — located 11 bp downstream of V_2. This variant was observed in more than 99% of proband sequences containing V_2 and in virtually none of the sequences containing the reference allele at this position, confirming that it is in *cis* relative to V_2 (and V_1 by inference). The V_3 variant was not observed in the parental sequences, confirming that it also arose de novo in the proband.

Plasmids and mutagenesis. Plasmids encoding human $Na_V1.6$ splice isoforms annotated by NCBI as variant 1 (NM_014191; neonatally expressed, $Na_V1.6N$) and variant 3 (NM_001177984; adult expressed, $Na_V1.6A$) were rendered stable in bacteria by inserting small introns at the exon 14-15 and 22-23 junctions, as described previously (47). Plasmids included an IRES2 element followed by the reading frame for the red fluorescent protein mScarlet to enable determination of transfection efficiency. Both plasmids are available from AddGene ($Na_V1.6N$, 162280; $Na_V1.6A$, 209411). *SCN8A* variants were introduced into WT $Na_V1.6A$ or $Na_V1.6N$ using PCR mutagenesis with Q5 Hot Start High-Fidelity 2× Master Mix (New England Biolabs), as described previously (47). Primers were designed for each mutation using custom software to have a minimum 5′ overlap of 20 bp and a predicted melting temperature (Tm) of 60°C (Supplemental Table 4). All recombinant plasmids were sequenced in their entirety using nanopore-based sequencing (Primordium Labs) to confirm the presence of the desired modifications and the absence of inadvertent mutations.

Cell culture. ND7/23 (Sigma-Aldrich) and ND7/LoNav (see below) cells were grown at 37°C with 5% CO_2 in Dulbecco's modified Eagle's medium (DMEM) supplemented with 10% fetal bovine serum (ATLANTA Biologicals), 2 mM L-glutamine, 50 U/mL penicillin, and 50 μg/mL streptomycin. Unless otherwise stated, all tissue culture media were obtained from Thermo Fisher Scientific.

Generation of ND7/LoNav cells. Transient knockdown of $Na_V1.7$ mRNA was done using short interfering RNA (siRNA) targeting both mouse and rat channel transcripts (4390771, ID: s134909; Thermo Fisher Scientific/Ambion). Permanent knockout of endogenous $Na_V1.7$ in ND7/23 cells was achieved using CRISPR/Cas9 genome editing with plasmid pD1301-AD (pCMV-Cas9-2A-GFP) encoding a guide RNA (gRNA) sequence (GTTACTGCTGCGCCGCTCCC) targeting both mouse *Scn9a* (GRCM39, chr2:66370779–66370798) and rat *Scn9a* (mRatBN7.2, chr3:51197912–51197931). Genome-editing vectors were synthesized by ATUM. ND7/23 cells were transfected with FuGENE 6 Transfection Reagent (Promega) according to the manufacturer's instructions. Two days after transfection, cells were flow sorted and green fluorescent cells with the top 50% intensity were isolated for single-clone selection. Sequencing of PCR amplicons encompassing the edited regions that were subcloned into the TOPO-TA vector (Invitrogen) revealed a subset with in-frame deletions in mouse *Scn9a*. An additional round of CRISPR/Cas9 genome editing was performed on 1 clonal cell line to further disrupt the coding region of endogenous *Scn9a* using recombinant pX458 plasmid (pSpCas9-2A-GFP; Addgene, 48138) and a gRNA targeting the in-frame deletion (*Scn9a*, CTATTTGTACCCCATAAG). After transfection and flow sorting of green fluorescent cells, clonal lines with the lowest inward current amplitude determined by whole-cell automated patch clamp recording were selected.

Immunoblotting. Mouse and rat $Na_V1.6$ and $Na_V1.7$ were detected using anti-$Na_V1.6$ antibody (1:100 dilution; ASC-009, Alomone Labs) and anti-$Na_V1.7$ antibody (1:200 dilution; 75-103, UC Davis/NIH NeuroMab Facility), respectively. Transferrin receptor (loading control) was detected with mouse anti–human transferrin receptor antibody (1:500; 136800, Invitrogen). Protein samples (50 μg) were electrophoresed in 7.5% polyacrylamide Mini-PROTEAN TGX gels (4561023, Bio-Rad), electrotransferred to Immobilon-P PVDF membranes (pore size 0.45 μm, IPFL00010, MilliporeSigma), and blocked in 5% bovine serum albumin for 1 hour. Sodium channels were detected by first incubating with anti-$Na_V1.6$ or -$Na_V1.7$ primary antibodies followed by incubation with IRDye 800CW goat anti-mouse antibody (1:10,000; 926-322100, LI-COR Biosciences). Transferrin receptor was detected with primary antibody followed by incubation with IRDye 680RD goat anti-mouse antibody (1:10,000; 926-68070, LI-COR Biosciences). Protein bands were imaged with the Odyssey CLx Imaging System (LI-COR Biosciences).

Transfections. WT and variant human $Na_V1.6A$ and $Na_V1.6N$ plasmids were transiently expressed in ND7/LoNav cells using the STX system (MaxCyte Inc.). ND7/LoNav cells were seeded at 1.1×10^6 cells/mL in 100-mm tissue culture dishes and grown to 65%–75% density, and then harvested using TrpLE Express (12605010, Thermo Fisher Scientific/GIBCO). A 500 μL aliquot of cell suspension was used to determine cell number and viability using an automated cell counter (ViCell, Beckman Coulter). Remaining cells were collected by gentle centrifugation (160*g*, 4 minutes), washed with 5 mL electroporation buffer (EBR100, MaxCyte Inc.), and resuspended in electroporation buffer at a density of 1×10^8 viable cells/mL. Each electroporation was performed using 100 μL of cell suspension.

ND7/LoNav cells were electroporated with 50 μg of WT or variant $Na_V1.6$ cDNA. The DNA-cell suspension mix was transferred to an OC-100 processing assembly (MaxCyte Inc.) and electroporated using the preset Optimization 4 protocol. Immediately after electroporation, 10 μL of DNase I (Sigma-Aldrich) was added to the DNA-cell suspension. Cell-DNA-DNase mixtures were transferred to 6-well tissue culture plates and incubated for 30 minutes at 37°C in 5% CO_2. Following incubation, cells were gently resuspended in culture media, transferred to 100-mm tissue culture dishes, and grown for 48 hours at 37°C in 5% CO_2. Following incubation, cells were harvested, counted, transfection efficiency determined by flow cytometry (see below), and then frozen in 1 mL aliquots at 1.8×10^6 viable cells/mL in liquid nitrogen until used in experiments. Mean transfection efficiency was 82%, and only batches of cells exhibiting an efficiency of greater than 65% were used in experiments.

Transfection efficiency was evaluated by flow cytometry using a FACSCanto (BD Biosciences) located in the Northwestern University Interdepartmental Immunobiology Flow Cytometry Core Facility. Forward scatter, side scatter, and red fluorescence were measured using a 488 nm laser.

Manual patch clamp recording. Currents were recorded at room temperature in the whole-cell configuration while acquired at 20 kHz and filtered at 5 kHz. Bath solution contained (in mM): 145 NaCl, 4 KCl, 1.8 $CaCl_2$, 1 $MgCl_2$, 10 HEPES, pH 7.35, and 310 mOsm/kg. The composition of the pipette solution was (in mM): 10 NaF, 110 CsF, 20 CsCl, 2 EGTA, 10 HEPES, pH 7.35, 310 mOsm/kg. Whole-cell patch pipettes were pulled from thin-wall borosilicate glass (Warner Instruments, LLC) with a multistage P-97 Flaming-Brown micropipette puller (Sutter Instruments Co.) and fire-polished with a Micro Forge MF 830 (Narashige International). Pipette resistance was approximately 2 MΩ.

Cell preparation for automated electrophysiology. Electroporated cells were thawed the day before experiments, plated in 60-mm tissue culture dishes, and incubated for 18–24 hours at 37°C in 5% CO_2.

Prior to experiments, cells were detached using TrpLE Express, resuspended in cell culture media, and counted. Cells were centrifuged at 100*g* for 2 minutes and then resuspended at 180,000/mL with external solution (see below) and allowed to recover 45 minutes at 15°C while shaking 200 rpm on a rotating platform.

Automated patch clamp. Automated planar patch clamp recording was performed using a SyncroPatch 768 PE (Nanion Technologies), as previously described (28). External solution contained (in mM): 140 NaCl, 4 KCl, 2.0 $CaCl_2$, 1 $MgCl_2$, 10 HEPES, 5 glucose, pH 7.4. The composition of the internal solution was (in mM): 10 NaF, 110 CsF, 10 CsCl, 20 EGTA, 10 HEPES, pH 7.2. Whole-cell currents were acquired at 10 kHz and filtered at 3 kHz. The access resistance and apparent membrane capacitance were determined. Series resistance was compensated 90%, whereas leak and capacitance artifacts were subtracted using the P/4 method.

Data were analyzed and plotted using a combination of DataController384 version 1.8 (Nanion Technologies), Excel (Microsoft Office 2013, Microsoft), SigmaPlot 2000 (Systat Software, Inc.), and Prism 8 (GraphPad Software), as previously described (28). Whole-cell currents were measured from a holding potential of –120 mV. Whole-cell conductance (G_{Na}) was calculated as $G_{Na} = I/(V - E_{rev})$, where I is the measured peak current, V is the step potential, and E_{rev} is the calculated sodium reversal potential. G_{Na} at each voltage step was normalized to the maximal conductance between −80 mV and 20 mV. To calculate voltage dependence of activation and inactivation, data were plotted against voltage and fitted with Boltzmann functions. Time-dependent recovery from inactivation was evaluated by fitting peak current recovery with a 2-exponential function. Time-dependent entry into inactivation was evaluated by fitting current decay at 0 mV with a single exponential function. Number of cells (n) is given in the figure legends. Persistent current was measured as the ratio of peak ramp current to the peak current measured at 0 mV during the activation protocol, and charge movement was calculated as the integral of the ramp current divided by the current measured during the activation protocol. Window current was calculated by integrating the area under the intersection between the Boltzmann fits for voltage dependence of activation and inactivation using a custom MatLab script (48).

Statistics. Data from individual cells expressing variant $Na_V1.6$ were compared to the average of the isoform-matched WT $Na_V1.6$ run in parallel using a 2-tailed t test. Statistical significance was established at a P value of 0.01 or less, which represents a Bonferroni's correction for multiple testing in experiments comparing 4 variants to WT channels. One-way ANOVA was used to compare functional properties of WT $Na_V1.6$ splice isoforms and nontransfected cells, with statistical significance set at a P value of 0.01 or less. Unless otherwise noted, data are presented as mean ± 95% confidence intervals (CIs).

Study approval. For unpublished *SCN8A* variants, we obtained informed consent from parents to allow publication of brief deidentified clinical descriptions and genetic information using a method approved by the Children's Hospital of Philadelphia Institutional Review Board.

Data availability. The authors confirm that the data supporting the findings of this study are available within the article and the supplemental material, including Supplemental Data Sets and the Supporting Data Values file.

Author contributions

CGV, TVA, JMD, NFG, MJO, CBB, and CHT performed experimental work and analyzed data. IH acquired informed consent. ALG acquired funding and supervised the work. The manuscript was written primarily by CGV and ALG, with input from all co-authors. All authors reviewed and approved the final version of the manuscript prior to submission.

Acknowledgments

This study was funded by a grant from the National Institute for Neurological Diseases and Stroke (NS108874).

Address correspondence to: Alfred L. George Jr., Department of Pharmacology, Northwestern University Feinberg School of Medicine, Searle 8-510, 320 E. Superior St., Chicago, Illinois 60611, USA. Phone: 312.503.4893; Email: al.george@northwestern.edu.

---

1. Lindy AS, et al. Diagnostic outcomes for genetic testing of 70 genes in 8565 patients with epilepsy and neurodevelopmental disorders. *Epilepsia*. 2018;59(5):1062–1071.
2. Brunklaus A, et al. Biological concepts in human sodium channel epilepsies and their relevance in clinical practice. *Epilepsia*. 2020;61(3):387–399.
3. Knowles JK, et al. Precision medicine for genetic epilepsy on the horizon: recent advances, present challenges, and suggestions

for continued progress. *Epilepsia*. 2022;63(10):2461–2475.

4. Brunklaus A, et al. Prophecy or empiricism? Clinical value of predicting versus determining genetic variant functions. *Epilepsia*. 2023;64(11):2909–2913.
5. Meisler MH, et al. SCN8A encephalopathy: research progress and prospects. *Epilepsia*. 2016;57(7):1027–1035.
6. Johannesen KM, et al. The spectrum of intermediate SCN8A-related epilepsy. *Epilepsia*. 2019;60(5):830–844.
7. Ye M, et al. Differential roles of $Na_V1.2$ and $Na_V1.6$ in regulating neuronal excitability at febrile temperature and distinct contributions to febrile seizures. *Sci Rep*. 2018;8(1):753.
8. Copley RR. Evolutionary convergence of alternative splicing in ion channels. *Trends Genet*. 2004;20(4):171–176.
9. Liang L, et al. Developmental dynamics of voltage-gated sodium channel isoform expression in the human and mouse brain. *Genome Med*. 2021;13(1):135.
10. Epilepsy Genetics Initiative. De novo variants in the alternative exon 5 of SCN8A cause epileptic encephalopathy. *Genet Med*. 2018;20(2):275–281.
11. Veeramah KR, et al. De novo pathogenic SCN8A mutation identified by whole-genome sequencing of a family quartet affected by infantile epileptic encephalopathy and SUDEP. *Am J Hum Genet*. 2012;90(3):502–510.
12. de Kovel CG, et al. Characterization of a de novo SCN8A mutation in a patient with epileptic encephalopathy. *Epilepsy Res*. 2014;108(9):1511–1518.
13. Wagnon JL, et al. Pathogenic mechanism of recurrent mutations of SCN8A in epileptic encephalopathy. *Ann Clin Transl Neurol*. 2016;3(2):114–123.
14. Patel RR, et al. Aberrant epilepsy-associated mutant Nav1.6 sodium channel activity can be targeted with cannabidiol. *Brain*. 2016;139(pt 8):2164–2181.
15. Zaman T, et al. A single-center SCN8A-related epilepsy cohort: clinical, genetic, and physiologic characterization. *Ann Clin Transl Neurol*. 2019;6(8):1445–1455.
16. Liu Y, et al. Neuronal mechanisms of mutations in SCN8A causing epilepsy or intellectual disability. *Brain*. 2019;142(2):376–390.
17. Pan Y, Cummins TR. Distinct functional alterations in SCN8A epilepsy mutant channels. *J Physiol*. 2020;598(2):381–401.
18. Bayraktar E, et al. In vitro effects of eslicarbazepine (S-licarbazepine) as a potential precision therapy on SCN8A variants causing neuropsychiatric disorders. *Br J Pharmacol*. 2023;180(8):1038–1055.
19. Lyu H, et al. Clinical and electrophysiological features of SCN8A variants causing episodic or chronic ataxia. *EBioMedicine*. 2023;98:104855.
20. Liu Y, et al. A SCN8A variant associated with severe early onset epilepsy and developmental delay: loss- or gain-of-function? *Epilepsy Res*. 2021;178:106824.
21. Johannesen KM, et al. Genotype-phenotype correlations in SCN8A-related disorders reveal prognostic and therapeutic implications. *Brain*. 2022;145(9):2991–3009.
22. Dunn PM, et al. Bradykinin evoked depolarization of a novel neuroblastoma x DRG neurone hybrid cell line (ND7/23). *Brain Res*. 1991;545(1–2):80–86.
23. Yin K, et al. Neuronal cell lines as model dorsal root ganglion neurons: a transcriptomic comparison. *Mol Pain*. 2016;12:1744806916646111.
24. Lee J, et al. NaV1.6 and NaV1.7 channels are major endogenous voltage-gated sodium channels in ND7/23 cells. *PLoS One*. 2019;14(8):e0221156.
25. Rogers M, et al. Characterization of endogenous sodium channels in the ND7-23 neuroblastoma cell line: implications for use as a heterologous ion channel expression system suitable for automated patch clamp screening. *Assay Drug Dev Technol*. 2016;14(2):109–130.
26. Poulin H, Chahine M. R1617Q epilepsy mutation slows $Na_V1.6$ sodium channel inactivation and increases the persistent current and neuronal firing. *J Physiol*. 2021;599(5):1651–1664.
27. Truty R, et al. Possible precision medicine implications from genetic testing using combined detection of sequence and intragenic copy number variants in a large cohort with childhood epilepsy. *Epilepsia Open*. 2019;4(3):397–408.
28. Thompson CH, et al. Epilepsy-associated SCN2A (NaV1.2) variants exhibit diverse and complex functional properties. *J Gen Physiol*. 2023;155(10):e202313375.
29. Vanoye CG, et al. High-throughput functional evaluation of KCNQ1 decrypts variants of unknown significance. *Circ Genom Precis Med*. 2018;11(11):e002345.
30. Kang SK, et al. Spectrum of KV2.1 dysfunction in KCNB1-associated neurodevelopmental disorders. *Ann Neurol*. 2019;86:899–912.
31. Glazer AM, et al. High-throughput reclassification of SCN5A variants. *Am J Hum Genet*. 2020;107(1):111–123.
32. Ng CA, et al. High-throughput phenotyping of heteromeric human ether-à-go-go-related gene potassium channel variants can discriminate pathogenic from rare benign variants. *Heart Rhythm*. 2020;17(3):492–500.
33. Kozek KA, et al. High-throughput discovery of trafficking-deficient variants in the cardiac potassium channel $K_V11.1$. *Heart Rhythm*. 2020;17(12):2180–2189.
34. Vanoye CG, et al. Functional evaluation of human ion channel variants using automated electrophysiology. *Methods Enzymol*. 2021;654:383–405.
35. Vanoye CG, et al. High-throughput evaluation of epilepsy-associated KCNQ2 variants reveals functional and pharmacological heterogeneity. *JCI Insight*. 2022;7(5):e156314.
36. Glazer AM, et al. Arrhythmia variant associations and reclassifications in the eMERGE-III sequencing study. *Circulation*. 2022;145(12):877–891.
37. Baez-Nieto D, et al. Analysing an allelic series of rare missense variants of CACNA1I in a Swedish schizophrenia cohort. *Brain*. 2022;145(5):1839–1853.
38. Jiang C, et al. A calibrated functional patch-clamp assay to enhance clinical variant interpretation in KCNH2-related long QT syndrome. *Am J Hum Genet*. 2022;109(7):1199–1207.
39. Quinn S, et al. Complex biophysical changes and reduced neuronal firing in an SCN8A variant associated with developmental delay and epilepsy. *Biochim Biophys Acta Mol Basis Dis*. 2024;1870(5):167127.
40. Gazina EV, et al. Differential expression of exon 5 splice variants of sodium channel alpha subunit mRNAs in the developing

mouse brain. *Neuroscience*. 2010;166(1):195–200.

41. Thompson CH, et al. Alternative splicing potentiates dysfunction of early-onset epileptic encephalopathy SCN2A variants. *J Gen Physiol*. 2020;152(3):e201912442.
42. Sergeeva OV, et al. Modulation of RNA splicing by oligonucleotides: mechanisms of action and therapeutic implications. *Nucleic Acid Ther*. 2022;32(3):123–138.
43. Cummins TR, et al. Nav1.3 sodium channels: rapid repriming and slow closed-state inactivation display quantitative differences after expression in a mammalian cell line and in spinal sensory neurons. *J Neurosci*. 2001;21(16):5952–5961.
44. Ben-Shalom R, et al. NeuroGPU: accelerating multi-compartment, biophysically detailed neuron simulations on GPUs. *J Neurosci Methods*. 2022;366:109400.
45. Berecki G, et al. Dynamic action potential clamp predicts functional separation in mild familial and severe de novo forms of *SCN2A* epilepsy. *Proc Natl Acad Sci U S A*. 2018;115(24):E5516–E5525.
46. Berecki G, et al. Functional correlates of clinical phenotype and severity in recurrent SCN2A variants. *Commun Biol*. 2022;5(1):515.
47. DeKeyser JM, et al. Cryptic prokaryotic promoters explain instability of recombinant neuronal sodium channels in bacteria. *J Biol Chem*. 2021;296:100298.
48. Ganguly S, et al. Enhanced slow inactivation contributes to dysfunction of a recurrent SCN2A mutation associated with developmental and epileptic encephalopathy. *J Physiol*. 2021;599(18):4375–4388.